Progress In Electromagnetics Research M, Vol. 64, 65–76, 2018

A Matching-Pursuit Based Approach for Detecting and Imaging Breast Cancer Tumor

Mustafa B. Bicer, Ali Akdagli*, and Caner Ozdemir

Abstract—In this study, the scattering map of the breast is reconstructed by applying the matching-pursuit algorithm (MPA) to the simulation data obtained by the monostatic inverse synthetic aperture radar (ISAR) principle, and the locations of the tumors are determined by considering the peaks on the scattering map. The MPA iteratively searches the true solution by assuming every discrete point in the solution space to be a scattering center by dividing the imaging region onto a discrete grid. In order to obtain images with better resolution, the fine granularity of the grid for accurate solutions is provided at the expense of increased processing times. First, our approach based on MPA is tested on simulated data generated by MATLAB for breast tumor detection and imaging. Perfect reconstruction for the locations of the hypothetical breast tumor points is attained. Then, a full-wave electromagnetic simulation software named CST Microwave Studio (CST MWS) is used to generate backscattered electric field data from a constructed scenario in which a tumor is located in a breast model. Next, we use the collected data from the defined scenarios as an input to our algorithm. Resultant images provide successful detection and imaging of the tumor region within the breast model. The accuracy of the MATLAB and the CST MWS simulation results demonstrate the availability of our MPA-based focusing algorithm to be used effectively in medical imaging.

1. INTRODUCTION

It is well known that breast cancer has the highest incidence among women all around the world [1–3]. Although it is a gradually growing disease, it causes death of the patient in the case of metastasize. Therefore, in the early stages of breast cancer, detection and diagnosis of breast tumor raise the chance of survival. Yet, the most effective applied technique for detecting and imaging the breast tumor is X-ray mammography [3, 4]. On the other hand, this method has two main drawbacks: the need to apply ionizing radioactive radiation and compress the breast that can be really uncomfortable and even painful. Although radiated X-rays are usually at low-power levels, same part of the body, i.e., chest region, cannot be scanned in short periods of time, which surely restricts the examination intervals of the patient. These disadvantages of the X-ray mammography technique led the researchers to explore new alternative methods such as magnetic resonance imaging (MRI) [3, 5] and ultrasound imaging (USI) [1, 3]. MRI is a magnetic resonance based imaging modality that eliminates the shortcomings o X-ray mammography and obtains highly resolved medical images. On the other hand, MRI is a relatively more expensive technique and provides lower specificity about the disease. Another method is the USI which is based on reconstructing the image using reflected sound waves from the breast. Although USI method looks more cost-effective compared to MRI, it has the same disadvantage of applying physical pressure to breast to let acoustic waves to better penetrate deeper regions. Furthermore, there is a need for employing coupling/matching gel which also creates an extra discomfort to the patient.

Received 12 October 2017, Accepted 14 January 2018, Scheduled 29 January 2018

* Corresponding author: Ali Akdagli (akdagli@mersin.edu.tr).
The authors are with the Department of Electrical and Electronics Engineering, Mersin University, Mersin, Turkey.

Above mentioned drawbacks have been the motivation for the researchers to work on detection/imaging algorithms based on metabolic changes and various tissue characteristics such as elasticity, temperature, optical properties and electromagnetic conductivity/permittivity. Studies on imaging the biological matters, especially breast tissues, based on the electric permittivity feature have gained acceleration in the last decades [6, 7]. Recent studies have revealed that the dielectric constant value of a diseased tissue is much higher than that of the healthy one in microwave frequencies [6, 7]. Therefore, this substantial contrast between the healthy and unhealthy tissues constitutes a basis for the microwave detection/imaging techniques. It has been reported by various researchers that these techniques have the advantages of being cheaper, providing comfortable employment of the scanning process and ease in application that can apparently mitigate the drawbacks of the above mentioned technologies [8–13]. Furthermore, using low power and providing non-ionizing microwave radiation are also notable benefits of these tools.

In recent years, many studies have been completed on microwave imaging techniques. The studies on the diagnosis and imaging of breast cancer with microwave imaging tools can be classified as tomography-based and radar-based microwave imaging [10, 14–20]. Both methods use illumination of the breast with electromagnetic (EM) waves in the microwave frequency range and exploit the scattered signal for the detection and imaging. The scattered EM wave can provide various information such as physical size, distance from the skin, tumor and other tissues.

While tomography-based microwave imaging (TBMI) forms the dielectric scattering map of the breast, radar-based microwave imaging (RBMI) makes use of amplitude differences in the scattering signal and provides simple and powerful reconstructed amplitude-based images of the interested region. There are various numerical studies in the literature on diagnosis, detection and imaging of breast cancer with the use of microwave imaging such as circular [21] and indirect holographic reconstruction [22], confocal microwave imaging [13], multistatic adaptive microwave imaging [11], field mapping algorithm [23], hybrid reconstruction [24] and delay and sum procedures with various alternatives [8, 25]. In [21], fibroglangular tissue structures mimicking the real breast tissues are used in a rotating platform filled with impedance matching liquid, and the scattering waves acquired with the help of Vivaldi antennas are processed with the holographical imaging method. In study [22], a parabolic dish antenna is used to measure reflections from the breast phantom placed in oil at 9.4 GHz frequency. Also, a gun hidden in a bag and a Perspex tube are used in the measurements, and indirect holography method is applied. Fear et al. [13] used the method of confocal microwave imaging based on arrival times and amplitudes of scattering waves by acquiring data from the numerically modelled breast, and the breast tumor of 6 mm in size was imaged in three-dimensions.

In this study, the scattering map of the breast is formed by applying the matching-pursuit algorithm (MPA) to the simulation data obtained by employing the inverse synthetic aperture radar (ISAR) concept such that tumor locations are determined accordingly. The MPA is a powerful search algorithm that was previously applied in various fields such as recovering sparse signals in telecommunication systems and extracting the scattering centers in radar imaging [26–34]. In this work, we set out to develop an MPA-based focusing algorithm for detecting and imaging tumor tissues in the breast. The regions of the tumor locations are determined by considering the peak points in the reconstructed images produced by our algorithm. Firstly, the algorithm is applied to a case with a model composed of perfect point scatterers in MATLAB programming environment. Results obtained from MATLAB generated data have proved the validity and robustness of the proposed technique. Afterwards, the algorithm is tried with data gathered with a full-wave electromagnetic simulation software named CST Microwave Studio. It is demonstrated that our MPA based technique has the ability to successfully locate and image the modelled tumor structures within the breast model.

2. BREAST TUMOR DETECTION BASED ON MATCHING PURSUIT ALGORITHM

Our approach in detecting and localizing breast tumor is based on collecting the backscattered electromagnetic (EM) waves in monostatic inverse synthetic aperture radar (ISAR) configuration. As shown in Figure 1, the backscattered data are gathered in a circular manner around the perimeter of the breast for a total of N distinct multi-static measurements.

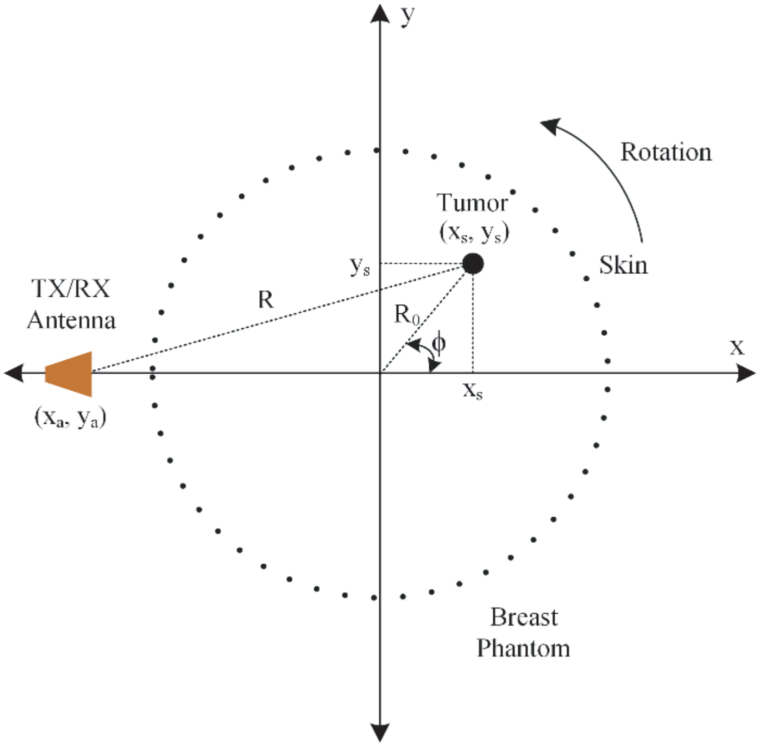

Figure 1. Simulation data derivation setup.

For the algorithm, we assume that the breast tissue is linear, homogeneous and isotropic. Provided that the main reflection from the air-to-breast skin is range-gated, any point inside the breast whose dielectric permittivity is different from that of the breast tissue will produce backscattered electric field in the frequency domain as follows [35]:

$$E_s(f,\phi) = A_0 e^{-j\left(\frac{4\pi f}{v}\right)R(\phi)} \tag{1}$$

where f, A_0 and ϕ represent the frequency, amplitude of the electric field and angle of the measurement location, respectively. The Euclidean distance R can be expressed in terms of the cylindrical angle variable ϕ as

$$R(\phi) = \sqrt{(x_a - R_0\cos\phi)^2 + (y_a - R_0\sin\phi)^2} \tag{2}$$

and phase velocity v is,

$$v = \begin{cases} c & \text{on air} \\ \dfrac{c}{\sqrt{\varepsilon_r}} & \text{inside breast} \end{cases} \tag{3}$$

where $(x_a,\ y_a)$, c, ε_r and R_0 denote the position of the antenna, velocity of the light in free space, dielectric constant of the medium, and tumor distance relative to the origin of the breast, respectively. For the sake of straightforwardness, we propose a simple breast model with ideal tumor structures of dielectrics such that tissue medium beneath the breast is considered homogeneous, linear and isotropic. Therefore, the tissue and tumors can be represented by different relative electric permittivity values.

As illustrated in Figure 1, the breast or the phantom is illuminated in the monostatic configuration while the antenna is moved on a circular path of a total of N distinct points that correspond to different look angle values of ϕ. The center of the circle is the breast's origin, and the radius of the measurement circle is about 1 to 3 centimeters greater than the actual radius of the breast or the phantom. The frequency-diverse backscattered electric field is collected at every discrete location such that we obtain a two-dimensional (2D) field data matrix in the frequency-aspect domain. Expectably, the resultant electric field data contain information about the skin and tumor points. Then, detection and reconstructing the scattering map of the breast containing tumors are carried out with the aid of MPA using the obtained data.

To be able to successfully detect and locate the tumors within the breast, collected electric field $E_s(f,\phi)$ with the help of N static measurements needs to be focused. Provided that there is a total of M point scatterers that may represent tumors inside the breast, the electric field in Eq. (1) is generalized to give

$$\begin{aligned} E_s\left(f,\phi\right) &= \sum_{i=1}^{M} E_i\left(f,\phi\right) \\ &= \sum_{i=1}^{M} A_i e^{-j\left(\frac{4\pi f}{v}\right)R_i(\phi)} \end{aligned} \tag{4}$$

where A_i and $R_i(\phi) = \sqrt{(x_a - R_{i0}\cos\phi)^2 + (y_a - R_{i0}\sin\phi)^2}$ represent the scattering amplitude and the distance from the radar for the ith point scatterer inside the breast. Here, R_{i0} represents the ith scattering point inside the breast. It is clear that the exact location of the ith scattering point, i.e., (x_{i0}, y_{i0}) equals the following:

$$(x_{i0}, y_{i0}) = (R_{i0}\cos\phi, R_{i0}\sin\phi) \tag{5}$$

It is obvious from Eq. (4) that the 2D Fourier relationship between the frequency-and-aspect and the tumor's x-and-y location does not provide a direct transformation because tumor's range distance varies as the radar's look angle changes. Therefore, direct inverse Fourier transformation will not yield a focused radar image of the scattering region within the breast region since the basis functions within the summation over angles in Eq. (4) are not orthogonal to each other. To overcome this problem, we adopt the well-known matching-pursuit algorithm (MPA) [26, 36] to extract the model parameters such as scattering amplitude and scattering location iteratively, and then reconstruct the scattering map of the breast.

In our approach to this problem, we rewrite Eq. (4) to have the model defined as the following:

$$E_s\left(f,\phi\right) = \sum_{i=1}^{M} A_i \cdot h_i\left(f,\phi,x_i,y_i\right) \tag{6}$$

Here, $h_i\left(f,\phi,x_i,y_i\right)$ is the basis function of the ith scattering center and given by

$$h_i\left(f,\phi,x_i,y_i\right) = e^{-j\left(\frac{4\pi f}{v}\right)\sqrt{\left(x_a-x_i\right)^2+\left(y_a-y_i\right)^2}} \tag{7}$$

Having the collected electric field as a function of frequency and aspect, our main aim is to determine a model that best approximates the collected electric field with as few scattering center points as possible. The unknown parameters are the position of the scattering location, (x_i, y_i), and the scattering amplitude, A_i.

The steps of our MPA implementation can be briefly expressed as follows:

(i) In each iteration of our MPA implementation, we project the collected backscattered electric field onto every possible scattering center basis over 2D imaging plane. The location that gives the largest projection is selected as the strongest scattering center. The search process can be expressed as

$$A = \max_{(x,y)}\left\{\left\langle E_s, h\left(f,\phi,x,y\right)\right\rangle\right\} \tag{8}$$

where the inner product is defined as [36],

$$\langle E_s, h\rangle = \iint\limits_{f\ \phi} E_s h^* d\phi df \tag{9}$$

Here, this inner product gives the maximum likelihood or the correlation between the measured scattered electric field E_s and the modelled base function h. Of course, this correlation becomes maximum when the search over x's and y's coincides with the real values of a scattered center location at (x_i, y_i). At this point, we record the values of (x_n, y_n) and A_n, and move to the second step.

(ii) In each iteration of our MPA implementation, the residual electric field matrix is obtained by subtracting the electric field data related to the strongest scattering center from the residual electric field matrix from the previous iteration as,

$$E_{n+1}\left(f,\phi\right)=E_{n}\left(f,\phi\right)-A_{n}h_{n} \tag{10}$$

where n represents the iteration number. Therefore, the highest scattering center is subtracted from the electric field data together with its basis function that is $A_n \cdot h_n(f,\phi,x_n,y_n)$. In the residual electric field, therefore, the amplitude (A_{n+1}) of the next scattering center at (x_{n+1},y_{n+1}) is surely less than the amplitude (A_n) current scattering center at (x_n,y_n).

(iii) The search for extracting the scattering center continues until all high-amplitude scattering centers are extracted from the electric field data, and the amplitude of the scattering centers reaches the noise floor of the collected electric field or a user defined value. At the end of this step, the search is terminated, and the extracted values of (A_n,x_n,y_n)'s are recorded.

3. NUMERICAL RESULTS

3.1. MATLAB Simulations

The geometry for the breast tumor scenario is illustrated in Figure 1. The values of the simulation parameters for this geometry are listed in Table 1. As listed in the table, we have considered three different scenarios: In scenario #1, there is one tumor; in scenario #2, there exist two distinct tumors, and in scenario #3, there are three tumors available within the breast as the locations of tumors are listed in cylindrical coordinates.

Table 1. Values for simulation parameters.

Parameter	**Value**		
Start Frequency	0.3 GHz		
Stop Frequency	8.5 GHz		
Number of Frequencies	165		
Skin Origin (r,ϕ)	(0, 0°)		
Skin Radius	8 cm		
Gap between Antenna and Skin	2 cm		
Measurement Angle Period	1°		
Skin Point Count	96		
Tumor Point Count	96		
Tumor Radius	1 cm		
	Scenario 1	Scenario 2	Scenario 3
Tumor Coordinates	(3.72 cm, 144.8°)	(3.72 cm, 144.8°)	(3.72 cm, 144.8°)
		(4.34 cm, −45.7°)	(4.34 cm, −45.7°)
			(3.07 cm, −189.0°)

The surface of the circular antenna layer is divided into 1452 triangular mesh cells to provide the initial edge length of 0.50 cm for fine meshing. For scenario #1, one tumor is located at (3.72 cm, 144.8°) and the amplitude of the electric field is taken as 3 V/m. In the scenario #2, two tumors are located at (3.72 cm, 144.8°) and (4.34 cm, −45.7°) with amplitude of 3 V/m and 2 V/m. Then, the tumors in the last scenario of #3 are located on (3.72 cm, 144.8°), (4.34 cm, −45.7°) and (3.07 cm, 189.0°) with amplitude of 3 V/m, 2 V/m and 1 V/m, respectively. The tumor amplitudes are selected differently from each other because of distinctiveness. The values used in the simulation are given in Table 1, and the given values are chosen optimally according to the results obtained in trial-and-error.

Because the selected points are exactly the same as mesh points, the algorithm finds the location of the tumor exactly the same as the location without any error. The triangular meshed surface of the imaging region is given in Figure 2.

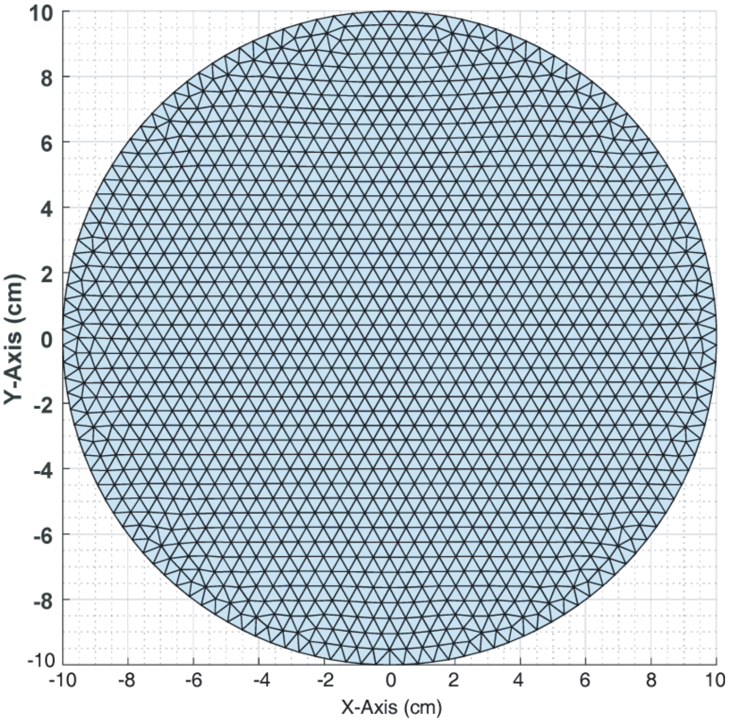

Figure 2. Meshed imaging region.

The initial edge length of the meshes given in Figure 2 is selected as 0.5 cm, and the region in circular area is meshed with 1452 triangular mesh nodes. In Figure 2, the boundaries on the X and Y axes represent the boundaries of the antenna layer as [−10 cm, 10 cm]. The mesh points and found tumor locations after applying the algorithm for scenario #3, which includes 3 tumors, are shown in Figure 3.

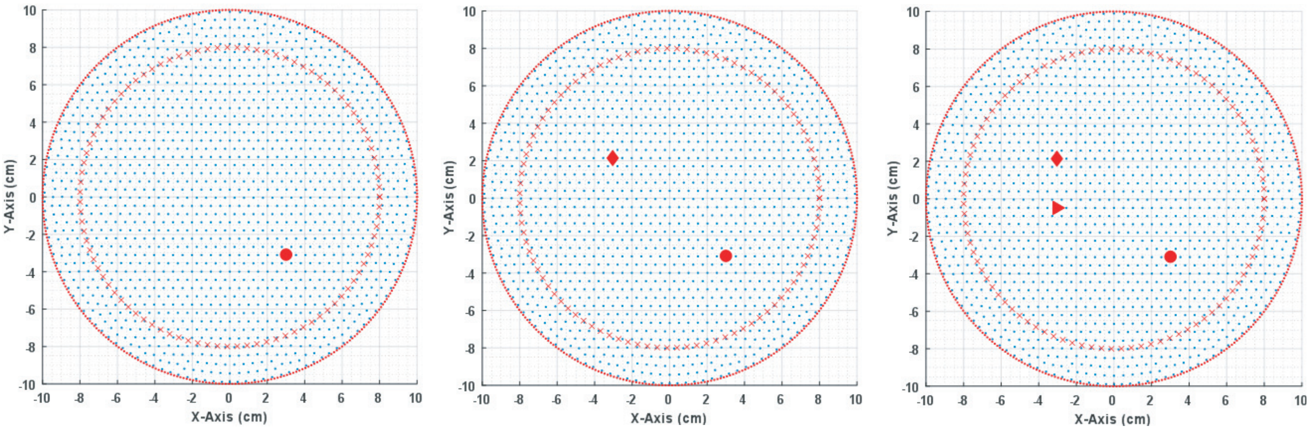

(a) (b) (c)

Figure 3. The meshed plots of mesh nodes, predicted tumor points, antenna layer and the skin layer (a) scenario #1, (b) scenario #2, (c) scenario #3.

Figure 3 shows the 1452 mesh nodes that are represented as blue dots. Furthermore, antenna measurement points are selected as 360, and each represents 1°. The breast skin is also represented by a total number of 96 perfect point scatterers. Three tumors in Figure 3 are denoted by three ideal point scatterers. Each mesh point is assumed as a tumor by MPA, and after applying the algorithm, the initial tumor locations are identified as points marked with red circles. Table 2 shows the original and predicted points, original and predicted amplitudes and percentage errors for amplitudes (PEA).

Table 2. Original and predicted tumor positions.

Scenarios	**Tumors**	**Original**		**Predicted**		**PEA (%)**
		Position (x, y) [cm]	**Amplitude (V)**	**Position**	**Amplitude**	
#1	Tumor #1	(−3.038, 2.142)	3	(−3.038, 2.142)	3.00	0.00
#2	Tumor #1	(−3.038, 2.142)	3	(−3.038, 2.142)	3.02	−0.66
	Tumor #2	(3.030, −3.110)	2	(3.030, −3.110)	2.00	0.00
#3	Tumor #1	(−3.038, 2.142)	3	(−3.038, 2.142)	3.12	−4.00
	Tumor #2	(3.030, −3.110)	2	(3.030, −3.110)	2.01	−0.50
	Tumor #3	(−3.035, −0.480)	1	(−3.035, −0.480)	0.99	−1.00

PEA: Error for Amplitude

According to the results of MPA given in Table 2, the algorithm determines the tumors at their exact locations perfectly in all three scenarios. However, the amplitudes for all tumors are calculated to have a maximum error margin about 4.00%. Also, MPA is utilized with various initial mesh edge lengths to generate the electric field map of scenario #3. The reconstructed images for scenario #3 using the predicted amplitudes are given in Figure 4.

As mentioned above, three tumors are located in scenario #3 and imaged inside the skin layer with some noise related to theoretical assumptions. As shown in Figure 4, the outer circle represents a layer of 360 antennas, and the points of the circle inside the antenna layer represent the skin points. The resolution of the reconstructed images is improved by decreasing the initial mesh edge lengths while the calculation time is increased. In Table 3, the total calculation time and the used initial edge length in mesh and related mesh points are tabulated.

As can be seen from Table 3, the count of total mesh points and total calculation time increases in a nonlinear manner. When the total calculation time and image resolutions are compared, the initial mesh edge length of 0.20 cm is acceptable, but 0.10 cm of edge length gives the best resolution for the simulation data.

Table 3. Performance change depending on the initial edge length of the mesh for scenario #3.

Mesh Initial Edge Length (unit)	**Mesh Point Count (piece)**	**Total Calculation Time (sec)**
0.50	1452	31
0.45	1788	38
0.40	2267	50
0.35	2955	63
0.30	4027	83
0.25	5809	125
0.20	9062	212
0.15	16114	401
0.10	36268	1178

Computing machine: Intel ® Xeon® CPU E5-2650 v3 @ 2.30 GHz (2 physical, 40 cores in total), 112 GB RAM

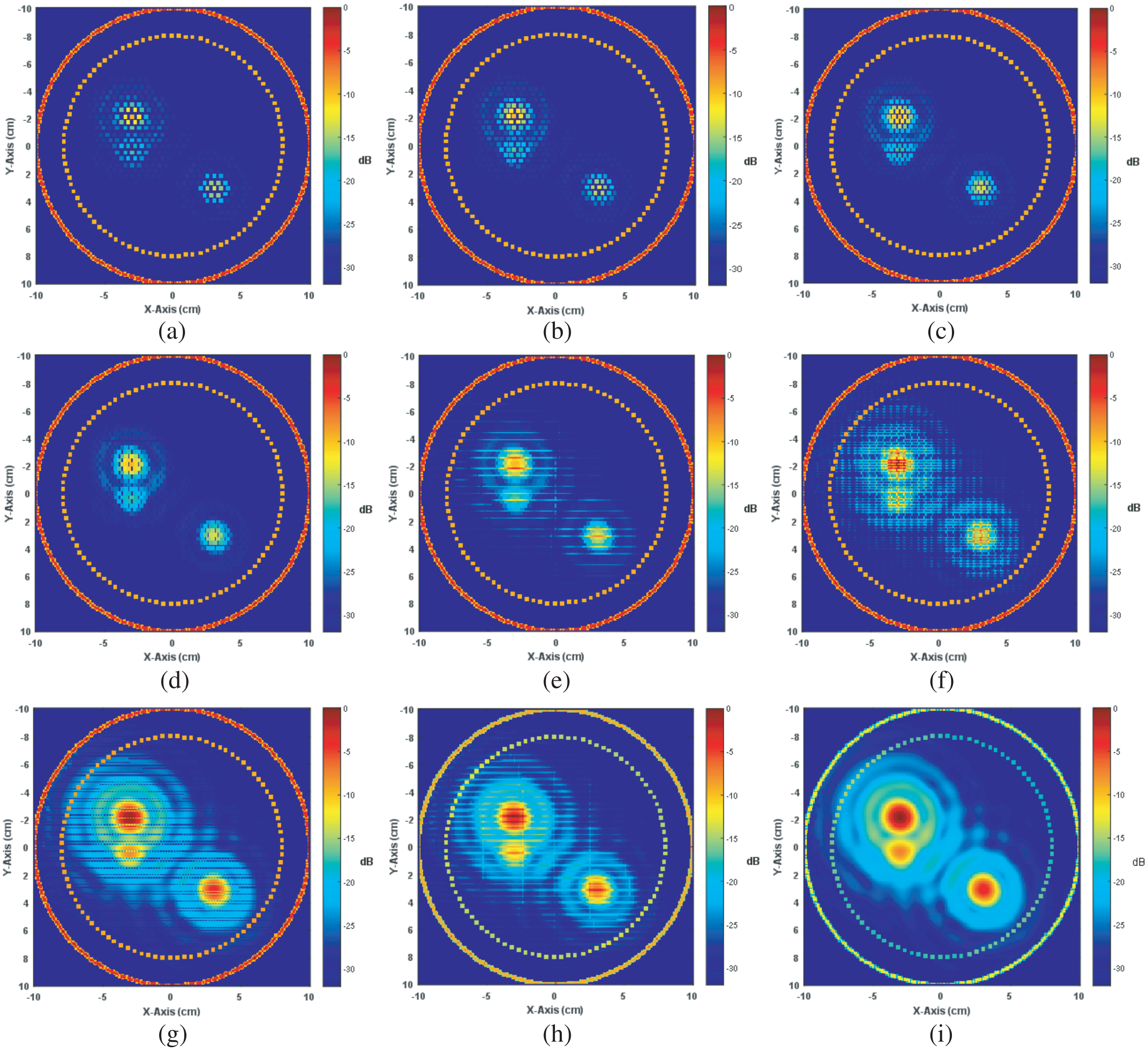

Figure 4. Reconstructed images of scenario #3 for various initial mesh edge granularities of (a) 0.50 cm, (b) 0.45 cm, (c) 0.40 cm, (d) 0.35 cm, (e) 0.30 cm, (f) 0.25 cm, (g) 0.20 cm, (h) 0.15 cm, (i) 0.10 cm.

3.2. CST MWS Simulations

In order to supply the MPA with more reliable data and validate the illustrations given in Figure 4, a realistic simulation study is carried out for the setup given in Figure 5 with the use of a full-wave electromagnetic simulation software, CST Microwave Studio [37].

The double-ridged horn antenna, shown in Figure 5, performs from 1 GHz to 16 GHz with an impedance bandwidth of less than -10 dB and placed 2 cm away from the object to be imaged. A half sphere with a radius of 7 cm with a dielectric constant of 4 as the healthy tissue and a sphere with a dielectric constant of 70 with a radius of 0.5 cm is constructed as the tumor structure in the simulation. The values of the parameters used in the simulation are given in Table 4.

The tumor structure is located in two different positions according to scenarios #4 and #5, respectively, and the simulations are done. The S_{11} parameters obtained as a result of the simulations are used as backscattered electric field data in imaging. The initial mesh granularity value is selected

(a) (b)

Figure 5. (a) Side view and (b) perspective view of the CST Microwave Studio simulation setup for scenario #5.

Table 4. Values for CST MWS simulation parameters.

Parameter	**Value**	
Start Frequency	1 GHz	
Stop Frequency	16 GHz	
Number of Frequencies	18	
Skin Radius	7 cm	
Gap between Antenna and Skin	2 cm	
Measurement Angle Period	5°	
Dielectric Value of Healthy Tissue	4	
Dielectric Value of Tumor Tissue	70	
Tumor Radius	1 cm	
Tumor Coordinates	Scenario 4	Scenario 5
	(2.7 cm, 325°)	(4.9 cm, 280°)

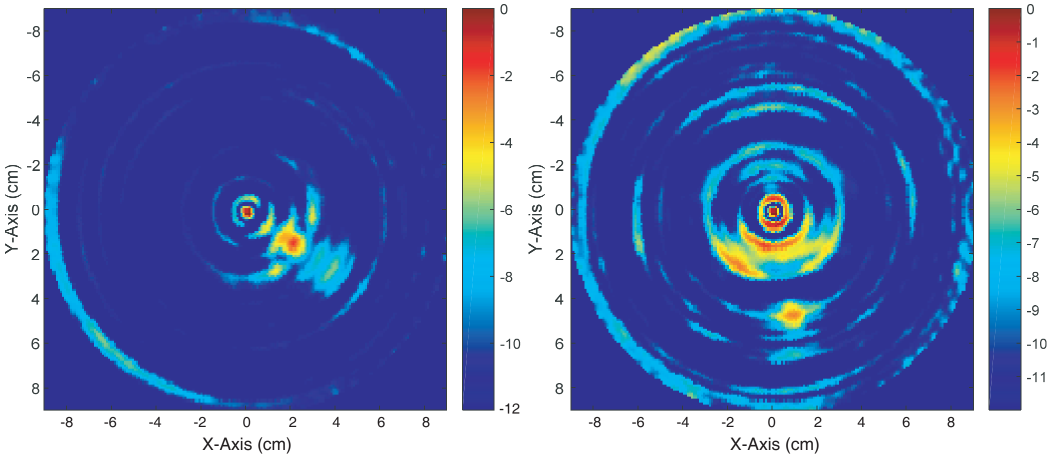

(a) (b)

Figure 6. Reconstructed images of (a) scenario #4 and (b) scenario #5 for initial mesh edge length of 0.08 cm.

as 0.08 cm, and the acquired simulation data are imaged with the use of MP algorithm. The obtained images are given in Figure 6. It can be seen from the figure that the tumor structures are obviously imaged at around 2.7 cm and 4.9 cm away from the origin. However, there are also artifacts and noises around the origin. The multi-reflections of the electromagnetic wave penetrating into the object and the power loss within the object can be regarded as the cause of these artifacts. To show the resultant images clearer and remove the artifacts, the amplitudes are scaled logarithmically, and the dynamic range of the display is selected as $-12\,\mathrm{dB}$.

4. CONCLUSION

In this study, scattering map of the imaging region, which consists of healthy breast tissues and tumor tissues in three different scenarios that have one, two and three tumors, respectively, is obtained. For this purpose, the breast phantom containing tumor tissue is discretized to derive simulation data based on the ISAR principle. Afterwards, the imaging region is divided into small triangular segments. Parametric studies on the dimensions of the mesh grids have also been carried out to improve the resolution of the reconstructed scattering map. Considering the optimum search time and resolution according to the triangular meshing approximation, dividing the imaging area into 1452 smaller grids related to 0.50 cm initial mesh edge length gives acceptable location information. It is observed that the resolution increases with the increase of the number of grids, but the search time is also increased. According to parametric studies on mesh grid sizes, 0.10 cm of initial mesh edge length gives the best resolution on reconstructed image. The further reduction of the value of this parameter does not provide any improvement due to the saturation of the image resolution. The highest peak values of the reconstructed image represent the tumor locations. In further studies, it is suggested to parallelize the algorithm to decrease the search time and increase the resolution.

ACKNOWLEDGMENT

This work was supported by Scientific Research Projects Department of Mersin University (Project No.: 2017-1-TP3-2190).

REFERENCES

1. Bicer, M. B., A. Akdagli, and C. Ozdemir, “Breast cancer detection using inverse radon transform with microwave image technique,” *2015 23th Signal Processing and Communications Applications Conference (SIU)*, 2182–2185, 2015.
2. Nass, S. J., I. C. Henderson, and J. C. Lashof, *Mammography and Beyond: Developing Technologies for the Early Detection of Breast Cancer*, Vol. 4, No. 3, National Academy Press, Washington, DC, 2002.
3. Kuhl, C. K., et al., “Mammography, breast ultrasound, and magnetic resonance imaging for surveillance of women at high familial risk for breast cancer,” *J. Clin. Oncol.*, Vol. 23, No. 33, 8469–8476, Nov. 2005.
4. Heywang-Köbrunner, S. H., A. Hacker, and S. Sedlacek, “Advantages and disadvantages of mammography screening,” *Breast Care*, Vol. 6, No. 3, 199–207, Jun. 2011.
5. Orel, S. G. and M. D. Schnall, “MR imaging of the breast for the detection, diagnosis, and staging of breast cancer,” *Radiology*, Vol. 220, No. 1, 13–30, Jul. 2001.
6. Lazebnik, M., D. Popovic, L. McCartney, C. B. Watkins, M. J. Lindstrom, J. Harter, S. Sewall, T. Ogilvie, A. Magliocco, T. M. Breslin, W. Temple, D. Mew, J. H. Booske, M. Okoniewski, and S. C. Hagness, “A large-scale study of the ultrawideband microwave dielectric properties of normal, benign and malignant breast tissues obtained from cancer surgeries,” *Phys. Med. Biol.*, Vol. 52, No. 20, 6093, 2007.
7. Surowiec, A. J., S. S. Stuchly, J. R. Barr, and A. Swarup, “Dielectric properties of breast carcinoma and the surrounding tissues,” *IEEE Transactions on Biomedical Engineering*, Vol. 35, No. 4, 257–263, 1988.
8. Lim, H. B., N. T. T. Nhung, E.-P. Li, and N. D. Thang, “Confocal microwave imaging for breast cancer detection: Delay-Multiply-and-Sum image reconstruction algorithm,” *IEEE Transactions on Biomedical Engineering*, Vol. 55, No. 6, 1697–1704, 2008.

9. Ortega-Palacios, R., L. Leija, A. Vera, and M. F. J. Cepeda, "Measurement of breast-tumor phantom dielectric properties for microwave breast cancer treatment evaluation," *Program and Abstract Book — 2010 7th International Conference on Electrical Engineering, Computing Science and Automatic Control, CCE 2010*, 216–219, 2010.
10. Li, X., E. J. Bond, B. D. Van Veen, and S. C. Hagness, "An overview of ultra-wideband microwave imaging via space-time beamforming for early-stage breast-cancer detection," *IEEE Antennas Propag. Mag.*, Vol. 47, No. 1, 19–34, 2005.
11. Xie, Y., B. Guo, L. Xu, J. Li, and P. Stoica, "Multistatic adaptive microwave imaging for early breast cancer detection," *IEEE Trans. Biomed. Eng.*, Vol. 53, No. 8, 1647–1657, 2006.
12. Fear, E. C., P. M. Meaney, and M. a Stuchly, "Microwaves for breast cancer detection," *IEEE Potentials*, Vol. 22, No. 1, 12, 2003.
13. Fear, E. C., X. Li, S. C. Hagness, and M. A. Stuchly, "Confocal microwave imaging for breast cancer detection: Localization of tumors in three dimensions," *IEEE Trans. Biomed. Eng.*, Vol. 49, No. 8, 812–822, 2002.
14. Winters, D. W., J. D. Shea, P. Kosmas, B. D. Van Veen, and S. C. Hagness, "Three-dimensional microwave breast imaging: Dispersive dielectric properties estimation using patient-specific basis functions," *IEEE Transactions on Medical Imaging*, Vol. 28, No. 7, 969–981, 2009.
15. Irishina, N., M. Moscoso, and O. Dorn, "Microwave imaging for early breast cancer detection using a shape-based strategy," *IEEE Trans. Biomed. Eng.*, Vol. 56, No. 4, 1143–1153, 2009.
16. Meaney, P. M., M. W. Fanning, T. Zhou, A. Golnabi, S. D. Geimer, and K. D. Paulsen, "Clinical microwave breast imaging — 2D results and the evolution to 3D," *Proceedings of the 2009 International Conference on Electromagnetics in Advanced Applications, ICEAA '09*, 881–884, 2009.
17. Kurrant, D. J., E. C. Fear, and D. T. Westwick, "Tumor response estimation in radar-based microwave breast cancer detection," *IEEE Transactions on Biomedical Engineering*, Vol. 55, No. 12, 2801–2811, 2008.
18. Davis, S. K., B. D. Van Veen, S. C. Hagness, and F. Kelcz, "Breast tumor characterization based on ultrawideband microwave backscatter," *IEEE Trans. Biomed. Eng.*, Vol. 55, No. 1, 237–246, 2008.
19. Yun, X., E. C. Fear, and R. H. Johnston, "Compact antenna for radar-based breast cancer detection," *IEEE Trans. Antennas Propag.*, Vol. 53, No. 8, 2374–2380, 2005.
20. Klemm, M., I. Craddock, J. Leendertz, A. Preece, and R. Benjamin, "Experimental and clinical results of breast cancer detection using UWB microwave radar," *2008 IEEE Antennas and Propagation Society International Symposium*, No. 1, 1–4, 2008.
21. Flores-Tapia, D., O. Maizlish, C. Alabaster, and S. Pistorius, "Microwave radar imaging of inhomogeneous breast phantoms using circular holography," *2012 9th IEEE International Symposium on Biomedical Imaging (ISBI)*, 86–89, 2012.
22. Smith, D., B. Livingstone, M. Elsdon, H. Zheng, V. Schejbal, and O. Yurduseven, "The development of indirect microwave holography for measurement and imaging applications," *2015 IEEE 15th Mediterranean Microwave Symposium (MMS)*, 1–4, 2015.
23. Cheng, G., Y. Zhu, and J. Grzesik, "3-D microwave imaging for breast cancer," *2012 6th European Conference on Antennas and Propagation (EUCAP)*, 3672–3676, 2011.
24. Pastorino, M., "Hybrid reconstruction techniques for microwave imaging systems," *2010 IEEE International Conference on Imaging Systems and Techniques*, 198–203, 2010.
25. Ünal, I., B. Türetken, and Y. Çotur, "Microwave imaging of breast cancer tumor inside voxel-based breast phantom using conformal antennas," *2014 31th URSI General Assembly and Scientific Symposium, URSI GASS 2014*,1–4, 2014.
26. Mallat, S. G. and Z. Zhang, "Matching pursuits with time-frequency dictionaries," *IEEE Transactions on Signal Processing*, Vol. 41, No. 12, 3397–3415, 1993.
27. Franaszczuk, P. J., G. K. Bergey, P. J. Durka, and H. M. Eisenberg, "Time-frequency analysis using the matching pursuit algorithm applied to seizures originating from the mesial temporal

lobe," *Electroencephalogr. Clin. Neurophysiol.*, Vol. 106, No. 6, 513–521, Jun. 1998.

28. Tropp, J. A. and A. C. Gilbert, "Signal recovery from random measurements via orthogonal matching pursuit," *IEEE Transactions on Information Theory*, Vol. 53, No. 12, 4655–4666, 2007.
29. La, C. and M. N. Do, "Tree-based orthogonal matching pursuit algorithm for signal reconstruction," *2006 International Conference on Image Processing*, 1277–1280, 2006.
30. Do, T. T., L. Gan, N. Nguyen, and T. D. Tran, "Sparsity adaptive matching pursuit algorithm for practical compressed sensing," *2008 42nd Asilomar Conference on Signals, Systems and Computers*, 581–587, 2008.
31. Pati, Y. C., R. Rezaiifar, and P. S. Krishnaprasad, "Orthogonal matching pursuit: Recursive function approximation with applications to wavelet decomposition," *Proceedings of 27th Asilomar Conference on Signals, Systems and Computers*, Vol. 1, 40–44, 1993.
32. Buhlmann, P., "Boosting for high-dimensional linear models," *Ann. Stat.*, Vol. 34, No. 2, 559–583, 2006.
33. Yoshida, H., R. M. Nishikawa, M. L. Giger, and K. Doi, "Signal/background separation by wavelet packets for detection of microcalcifications in mammograms," *Proc SPIE*, Vol. 2825, 2825–2827, 1996.
34. Moll, J., J. B. Harley, and V. Krozer, "Data-driven matched field processing for radar-based microwave breast cancer detection," *2015 9th European Conference on Antennas and Propagation (EuCAP)*, 1–4, 2015.
35. Ozdemir, C., *Inverse Synthetic Aperture Radar Imaging*, Wiley & Sons, Inc., Hoboken, NJ, 2012.
36. Su, T., C. Ozdemir, and H. Ling, "On extracting the radiation center representation of antenna radiation patterns on a complex platform," *Microw. Opt. Technol. Lett.*, Vol. 26, No. 1, 4–7, 2000.
37. CST Microwave Studio, Computer Simulation Technology GmbH.